metals

MDPI

Article

Effects of Post-Sinter Processing on an Al–Zn–Mg–Cu Powder Metallurgy Alloy

Matthew David Harding [1], Ian William Donaldson [2], Rich Lester Hexemer Junior [2] and Donald Paul Bishop [1,*]

[1] Department of Mechanical Engineering, Dalhousie University, Halifax, NS B3H 4R2, Canada; matthew.harding@dal.ca

[2] Advanced Engineering, GKN Sinter Metals LLC, Auburn Hills, MI 48326, USA; ian.donaldson@gkn.com (I.W.D.); rich.hexemer@gkn.com (R.L.H.J.)

* Correspondence: Paul.Bishop@dal.ca; Tel.: +1-902-494-1520

Received: 16 August 2017; Accepted: 8 September 2017; Published: 13 September 2017

Abstract: The objective of this work was to study the effects of several post-sinter processing operations (heat-treatment, sizing, shot peening) on a press-and-sinter 7xxx series aluminum powder metallurgy (PM) alloy. The characterization of the products was completed through a combination of non-contact surface profiling, hardness measurements, differential scanning calorimetry (DSC), transmission electron microscopy (TEM), X-ray diffraction (XRD), tensile, and three-point bend fatigue testing. It was determined that sizing in the as-quenched state imparted appreciable reductions in surface hardness (78 HRB) and fatigue strength (168 MPa) relative to counterpart specimens that were sized prior to solutionizing (85 HRB and 228 MPa). These declines in performance were ascribed to the annihilation of quenched in vacancies that subsequently altered the nature of precipitates within the finished product. The system responded well to shot peening, as this process increased fatigue strength to 294 MPa. However, thermal exposure at 353 K (80 °C) and 433 K (160 °C) then reduced fatigue performance to 260 MPa and 173 MPa, respectively, as a result of residual stress relaxation and in-situ over-aging.

Keywords: aluminum alloys; powder metallurgy; X-ray diffraction; fatigue; age hardening; residual stress; electron microscopy; thermomechanical processing; precipitation hardening

1. Introduction

Press-and-sinter aluminum powder metallurgy (PM) is an ever-growing industry due to the cost savings associated with high production rates and net shape capabilities coupled with the advantageous strength-to-weight ratio inherent to aluminum alloys. Much of this growth has been underpinned by the development of improved PM alloy formulations, with most lying within the general scope of 2xxx (Al–Cu–Mg) [1,2], 4xxx (Al–Si–Cu–Mg) [3], or 7xxx (Al–Zn–Mg–Cu) [4,5] chemistries. Accordingly, all such systems incorporate precipitation hardening as a key strengthening mechanism. Within this context, new aluminum PM alloys chemically compliant with the 7xxx series offer particularly high strength-to-weight ratios and are of natural commercial interest.

The traditional precipitation sequence believed to occur in wrought 7xxx series aluminum alloys was originally stated as [6]:

$$\text{SSSS} \rightarrow \text{GP-zone} \rightarrow \eta' \rightarrow \eta$$

Here, the metastable super saturated solid solution (SSSS) is formed upon quenching from the solutionization temperature. It then decomposes during natural or artificial aging, through the formation of clusters of solute atoms (so called Guinier–Preston (GP) zones) that eventually transform into the semi-coherent phase η′ and finally the fully incoherent phase η ($MgZn_2$). This precipitation

model is highly contested, and has been expanded upon with Ryum [7,8] proposing that hardening actually transpires through multiple reaction sequences:

$$\text{SSSS} \rightarrow \eta \qquad \alpha\text{-reaction}$$

$$\text{SSSS} \rightarrow \text{nuclei} \rightarrow \eta' \rightarrow \eta \qquad \beta\text{-reaction}$$

$$\text{SSSS} \rightarrow \text{GP-zone} \rightarrow \eta' \rightarrow \eta \qquad \gamma\text{-reaction}$$

In Ryum's model, all three precipitation reactions will take place upon aging the SSSS. The traditional model is retained in the γ-reaction, but additional sequences of the SSSS transforming directly to η (α-reaction) along with a tertiary reaction (β) occurring with discrete nuclei providing the precursor to η′ formation. Ryum believed that the nucleating agent was some manner of vacancy–solute atom aggregate. This model was further refined by Jiang et al. [9], who proposed the following:

$$\text{SSSS} \rightarrow \eta \qquad \alpha\text{-reaction}$$

$$\text{SSSS} \rightarrow \text{VRC} \rightarrow \text{GP-zone (II)} \rightarrow \eta' \rightarrow \eta \qquad \beta\text{-reaction}$$

$$\text{SSSS} \rightarrow \text{GP-zone (I)} \rightarrow \eta' \rightarrow \eta \qquad \gamma\text{-reaction}$$

Jiang believed that the nuclei identified by Ryum within the β-reaction were regions with a high concentration of quenched-in vacancies, and thereby denoted these as vacancy rich clusters (VRC). Such features then purportedly transform into GP-zone (II), which were identified as small regions enriched in vacancies and Zn atoms. It is notable that the GP-zone (I) phase found in the γ-reaction consists of regions high in solute atoms only, which differentiates it from GP-zone (II). Ryum believed that the β-reaction was the dominant sequence in alloys heat-treated to the T6 condition. Hansen et al. [10] concurred with this concept, and noted that peak strength occurred when the β-reaction was able to proceed until η′ became the dominant phase present while working with an Al–Zn–Mg–Zr alloy.

Beyond a standard heat-treatment practice of solutionization-quench-artificial aging, the post-sinter processing of aluminum PM products must also include a forming process so as to maintain appropriate dimensional tolerances within the final part. This step (termed "sizing") is typically completed at room temperature utilizing rigid tooling and press technology comparable to that used during powder compaction. While studies have looked into the mechanisms of sintering-induced distortion [11–13], there exists a clear void in the open literature on the effects of the actual sizing operation itself. Furthermore, the incorporation of post-sinter sizing and heat-treatment processes introduces the unique challenge of whether to apply sizing before, during, or after the heat-treatment cycle. For instance, if the sizing is applied prior to solutionization, any microstructural changes caused by the associated cold work would then be largely annihilated during heat-treatment, and the product may be prone to quench-induced distortion. Similarly, sizing may be implemented in between the quench and artificial aging steps so as to essentially apply a T8 temper. The benefits of a T8 treatment are that cold work is applied when the material is in a soft, malleable state, and that it can eliminate any distortion that may have occurred during quenching.

Although T8 treatments are common in certain aluminum alloys, they are rarely encountered when considering members of the 7xxx series. This largely stems from the dominant precipitation reactions that occur. For example, the θ-precipitation reaction present in the 2xxx series can benefit from cold working prior to artificial aging [14]. A detailed study of the influence of deformation immediately prior to aging on a wrought Al–Zn–Mg alloy [15] has shown that the introduction of dislocations by cold working will change the precipitation reaction upon aging, in some cases resulting in reduced mechanical properties. This is attributed to a reduced likelihood of η′ formation (the main strengthening phase) as a result of direct heterogeneous η formation on dislocations (likely a result of the α-reaction identified by Ryum and Jiang et al.).

Beyond sizing and heat-treatment, shot peening is another post-sinter operation of significant industrial impact, as it is known to increase fatigue performance. Shot peening is widely utilized across the majority of industries as a means to combat fatigue failure of metals by the introduction of a thin layer of compressive residual stress within the treated surface that helps to resist in-service tensile loads and in turn increase the fatigue performance. Studies have shown varying results for the effectiveness of shot peening to provide fatigue improvements within wrought AA7075. Was [16,17] conducted two studies considering the effects of shot peening on the fatigue strength of AA7075-T6, with no gains observed for tension–compression fatigue testing while increased fatigue strength was seen for reverse bending fatigue testing. Positive results were found by Benedetti et al. [18] and Wagner et al. [19] for reverse bending testing, while Honda et al. [20] found no improvements in fatigue strength during 3-point bend loading. In work by Harding et al. shot peening of PM7075 was found to impart positive results in rotating–bending fatigue performance, with gains of ~36% instilled through shot peening [21].

Overall, it is clear that post-sinter operations are a necessity within aluminum PM processing, yet detailed knowledge on how they affect the metallurgy of the final products remains largely non-existent within the open literature. Hence, the objective of this study was to initiate fundamental work in this area utilizing a commercially available 7xxx series powder mixture as the base material of interest.

2. Materials and Methods

The material of interest in this study was the commercially available aluminum PM system Alumix 431D produced by ECKA Granules (Fürth, Germany). Chemically, the system largely emulates wrought AA7075, but with the addition of a small amount of Sn to aid in sintering. Accordingly, it was denoted as PM7075 throughout this study. A complete assay for this PM system as measured by ICP-OES (Varian/Agilent Technologies, Santa Clara, CA, USA) is provided in Table 1. In addition to the PM system, wrought AA7075 (rolled plate) was also utilized in select instances for comparison purposes. The assay of this material relative to its respective nominal composition is also shown in Table 1.

Table 1. Measured assays of the raw materials utilized (weight %) relative to the nominal targeted chemistries.

Alloy	Assessment	Al	Cu	Fe	Mg	Si	Sn	Zn
PM7075	Target	Balance	1.6	-	2.5	-	0.2	5.5
	Measured	Balance	1.60	0.08	2.62	0.09	0.14	5.59
AA7075	Target	Balance	1.2–2.0	0.50	2.1–2.9	0.40	-	5.1–6.1
	Measured	Balance	1.55	0.66	2.05	0.14	-	5.44

All PM samples were produced by a standard press-and-sinter approach (i.e., die compaction of raw powder mixture followed by controlled atmosphere liquid phase sintering). Here, an array of test specimen geometries were fabricated, including Charpy bars (75 × 12.7 × 12.7 mm^3) for tensile testing, transverse rupture strength (TRS) bars (31.7 × 12.7 × 12.7 mm^3) for fatigue trials, and discs (30 mm diameter × 5 mm thick) for X-ray diffraction measurements. All samples were compacted in floating rigid die tooling at 400 MPa (pressurization rate of 10 MPa/s) and sintered in a continuous mesh belt furnace (BTU International, Inc., North Bellerica, MA, USA) under an atmosphere of high purity flowing nitrogen. The nominal thermal cycle consisted of a 20 minute dwell at 673 K (400 °C) for de-lubrication, followed by sintering at 878 K (605 °C) ± 5 K (5 °C) for 20 min and gas quenching to ambient temperature in a water-jacketed section of the furnace. During the sintering process, the atmospheric oxygen content was held at <10 ppm while the dew point was <213 K (−60 °C).

The sintered compacts then underwent secondary processing, which consisted of various combinations of heat-treatment, sizing, and shot peening. Table 2 provides a summary of the

specific sequences followed along with the notations utilized throughout this study. In all instances, solutionization was conducted at 743 K (470 °C) for 90 min at temperature followed by quenching into room temperature water. Artificial aging was completed at 398 K (125 °C) for 24 h to attain the T6 temper. Sizing was completed by uni-axially loading lubricated specimens within a closed die tool set. Shot peening was completed using an automated system to an intensity of 0.4 mmN (+5%/−0%) measured using standard N–S Almen strips before and after peening. The peening media was ZrO_2 with a shot diameter of 300 μm.

Table 2. Summary of the post-sinter processing sequences considered.

Notation	Processing Sequence
Sol-Age	Solutionize/quench/artificial aging
Sol-Size-Age	Solutionize/quench/size/artificial aging
Size-Sol-Age	Size/solutionize/quench/artificial aging
Size-Sol-Age-Peen	Size/solutionize/quench/artificial aging/shot peen

The characterization of the effects of sizing on the material began with measurements of percent reduction in thickness, density, surface roughness, and apparent hardness. The extent of sizing on samples was stated as a % reduction in height, with samples measured directly before and after sizing to 0.001 mm. Densities were measured by a standard Archimedes approach coupled with oil infiltration as per MPIF (Metal Powder Industries Federation) Standard 42 [22]. Surface topography was studied using a Micro-Profiler, model PS50 (Nanovea, Irvine, CA, USA), equipped with a 1.2 mm sensor. Data acquisition was completed using Nanovea 3D software with Nanovea Mountains Pro 3D (version 5.0, Nanovea, Irvine, CA, USA) used for all analyses, including that of surface roughness. Hardness measurements were completed in the Rockwell B scale (Buehler, Norwood, MA, USA) using a Wilson Rockwell 2000 unit.

The principal means of mechanical testing was fatigue. Here, TRS bars were first set in a 3-point bend fixture. Loading was then applied by a servo-hydraulic frame equipped with a 100 kN load cell. Testing was conducted at a frequency of 25 Hz, with a constant stress amplitude ratio of 0.1, and runout taken as 1,000,000 cycles. The staircase method was utilized with fatigue strength and standard deviation calculated based on MPIF Standard 56 [23]. A minimum of 10 tests were completed for each material processing condition of interest. To determine the tensile properties of specimens, Charpy bars were machined into threaded-end round tensile bars per ASTM E8M [24]. The bars were then tested in a 5594-200HVL (Instron, Norwood, MA, USA) hydraulic frame equipped with a 50 kN load cell. All specimens were loaded at a rate of 5 MPa/s, with strain data collected using an Epsilon model 3542 axial extensometer (Epsilontech, Jackson, MS, USA) that remained attached to the specimen through fracture. As such, the reported values for elongation represent the sum of elastic and plastic strain components.

Microstructural analyses included X-ray diffraction (XRD), differential scanning calorimetry (DSC), and transmission electron microscopy (TEM). XRD was undertaken using a D8 Advance (Bruker, Madison, WI, USA) operated with Co Kα radiation generated at an accelerating voltage of 35 kV and current of 27 mA. For residual stress measurements, the psi-splitting technique was followed with 11 psi-angles from −45° to 45° measured over the {331} aluminum peak. DSC (TA Instruments model SDT Q600, New Castle, DE, USA) was implemented to study precipitation hardening sequences. All such scans were conducted in air with a scanning rate of 5 K/min (5 °C/min) up to a maximum temperature of 773 K (500 °C). In each instance, an equivalent sample of high purity aluminum (99.999 wt % Al) was also scanned. The normalized data from the pure Al trace were subtracted from those acquired from test specimens in an effort to isolate the heat flow effects solely attributable to precipitation-based events. High magnification imaging of precipitates was completed by TEM using a Talos F200X scanning/transmission electron microscope (FEI, Hillsboro, OR, USA) operated with an accelerating voltage of 200 kV. TEM samples were mechanically ground and then electro-polished at

20 V with a solution of 30% HNO_3 in methanol cooled to 243 K (−30 °C). Representative bright field (BF) images and selected area diffraction patterns (SADPs) were recorded in each instance when the beam was closely aligned to the <112> zone axis.

3. Results and Discussion

3.1. Effects of Sizing on Physical Properties

Sizing is implemented in industry primarily for dimensional control, and it is typically stated as % reduction as defined by the thickness change before and after the sizing operation is completed. While the targeted amount of sizing can vary based on the tolerances required, the extent of sintering-induced distortion, and the geometry of the part in question, values are typically on the order of 3–5%. To identify suitable sizing pressures for PM7075, TRS bars were re-pressed at pressures ranging from 200 to 600 MPa. The Sol-Size-Age and Size-Sol-Age sequences were both evaluated in this manner, as significant differences in formability were anticipated. The effects of sizing pressure on the % reduction in thickness can be seen in Figure 1. Both sequences yielded clear and unique trends. The Sol-Size-Age sample showed an immediate rise in % reduction with increased sizing pressure before leveling off at a ~5.7% reduction in thickness for pressures ≥400 MPa. As would be expected, the Size-Sol-Age sample was more resilient to plastic deformation, with significantly higher pressures required to achieve a particular % reduction. Here, sizing pressures >300 MPa were needed to instill any meaningful level of permanent plastic set. The % reduction then rose gradually with a peak value of 5% realized at the highest pressure that could be safely evaluated (600 MPa). The astute differences in sizing behaviour were a direct consequence of fundamental differences in the yield strength and microstructure of the starting materials. In this sense, Size-Sol-Age samples were processed directly after sintering (T1 temper) whereby the material was in a naturally age-hardened state prior to sizing. The associated microstructure thereby included an abundance of precipitates derived from the η-based solid state reaction sequences [4]. By solutionizing the material immediately before sizing (Sol-Size-Age), the majority of these pre-existing strengthening features would have been eliminated, thereby softening the material and improving formability.

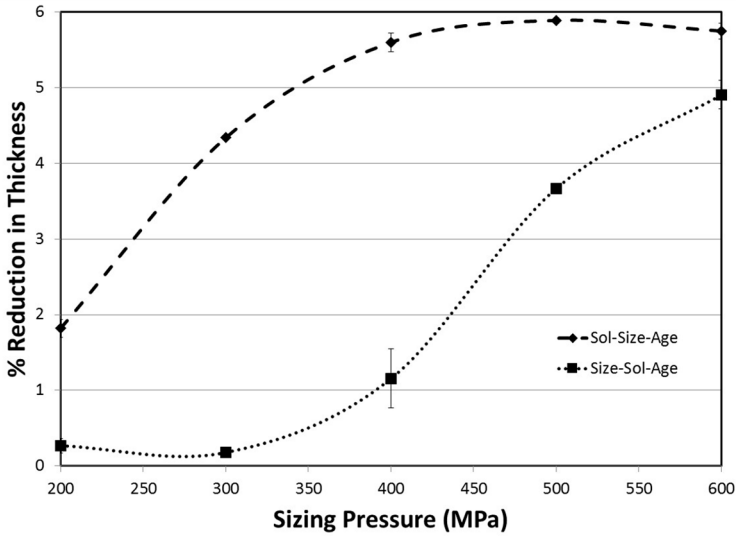

Figure 1. Effect of sizing pressure on % reduction in thickness for Sol-Size-Age and Size-Sol-Age processing sequences.

The effect of sizing pressure on the surface roughness of the material was also measured (Figure 2). A general decrease in this attribute was noted, with sizing pressure in both sequences resulting in smoother surfaces as compared to those present in the Sol-Age specimens (i.e., unsized).

The Sol-Size-Age products offered the lowest surface roughness for all sizing pressures other than 600 MPa, wherein parity with Size-Sol-Age products was observed. The differences here were again ascribed to microstructural differences within the starting materials, with Sol-Size-Age presenting a more formable system.

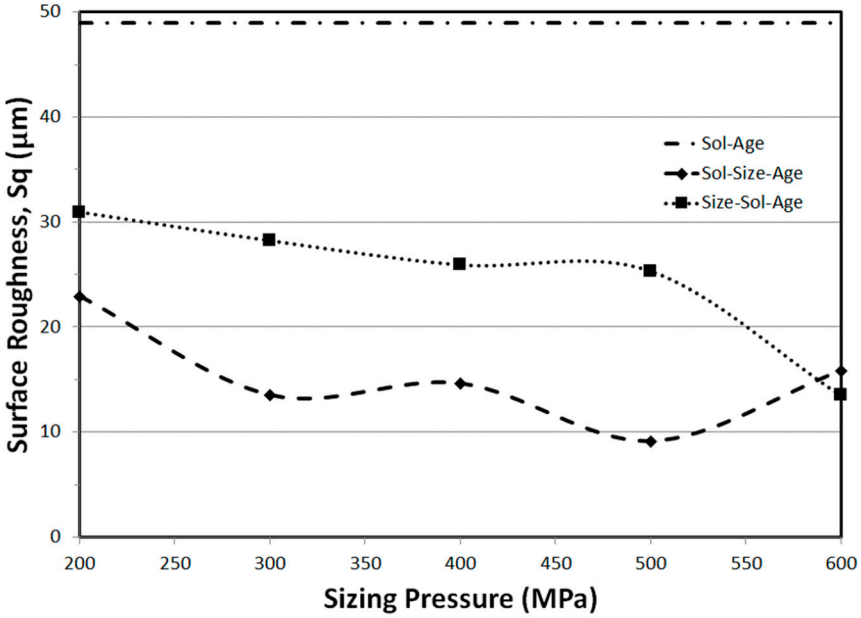

Figure 2. Effect of sizing pressure on surface roughness for Sol-Size-Age and Size-Sol-Age processing sequences.

Finally, the densities of numerous specimens in the Sol-Age, Sol-Size-Age, and Size-Sol-Age conditions were measured. Minimal differences were noted, as all values ranged from 2.77 to 2.78 g/cm^3 (representing 99.1–99.5% theoretical density) irrespective of sizing pressure. This was unsurprising, given that the material was almost fully dense in the sintered state (>99%) and that the deformation from sizing would be highly focused within a thin surface layer of the material. Based on the collective body of physical property data derived for the sized products, it was concluded that the sizing pressures required within the Sol-Size-Age and Size-Sol-Age sequences were 400 and 600 MPa, respectively. Under these conditions, the products from each stream were effectively equivalent in terms of % reduction (≈5%), surface roughness (≈15 µm), and density (≈2.775 g/cm^3).

3.2. Effects of Sizing on Mechanical Properties

3.2.1. Hardness

In the next stage of research, the effects of sizing on the mechanical properties of the finished products were considered, beginning with apparent hardness (Figure 3). In general, the hardness of the Size-Sol-Age specimens was largely unaffected by the extent of sizing, as all values hovered around the nominal measurement for the unsized, Sol-Age counterpart. However, the Sol-Size-Age samples showed a consistently lower hardness than both of these product forms, with the difference becoming more acute at sizing pressures >300 MPa.

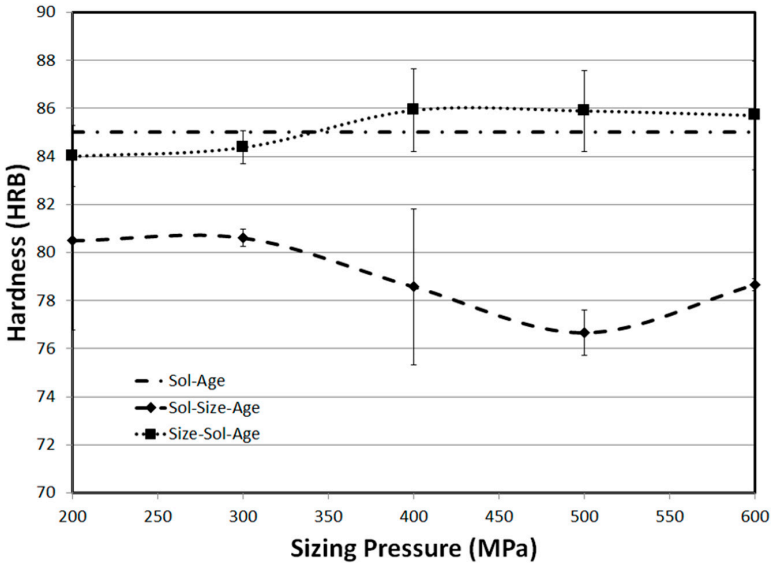

Figure 3. Effect of sizing pressure on apparent hardness for Sol-Size-Age and Size-Sol-Age processing sequences.

To determine if changes in the precipitates formed during age hardening may have been responsible for the trends in hardness data, pertinent information was gathered via DSC analyses. Here, samples were processed into the Sol-Size and Size-Sol states and heated in the DSC. In this approach, each specimen was thereby aged in-situ so as to accentuate the thermal events associated with any precipitation hardening mechanism(s) that were operative. The resultant heat flow traces are shown in Figure 4, with the principal peaks denoted A to D. With close consideration of the work by Ryum [7,8], Jiang et al. [9], Ghosh et al. [25], and Berg et al. [26], the precipitation events believed to be associated with these peaks (summarized in Table 3) were deduced. The first exothermic peak (A) was attributed to GP-zone (II) formation from vacancy rich clusters (VRC), which consist of regions enriched in vacancies and Zn atoms. It should be noted that GP-zone (I) (i.e., localized regions with heightened concentrations of Zn and Mg atoms) formation occurs at lower temperatures <323 K (50 °C) [9], which is why an exothermic peak corresponding to their formation was not observed in Figure 4. The second exothermic peak (B) was due to η′ and η formation/growth. Although some studies show discrete peaks associated with the formation of these two phases [9,27,28], these could not be distinguished in the present study. The endothermic peak (C) was identified as the dissolution of η′ and η, whereas peak (D) was ascribed to the melting of the S or T phase.

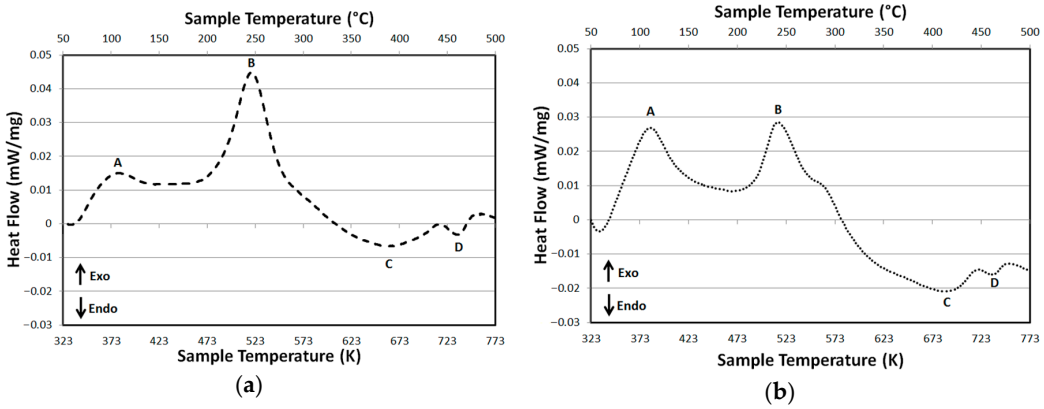

Figure 4. DSC (differential scanning calorimetry) scans recorded from samples of PM7075 (**a**) immediately after Sol-Size and (**b**) immediately after Size-Sol processing.

Table 3. Summary of the precipitation events observed in Sol-Size and Size-Sol processed specimens.

Peak	Event Description	Temperature K (°C)	
		Sol-Size	Size-Sol
A	GP [1]-zone (II) formation and growth	381 (108)	382 (109)
B	η′ and η formation	519 (246)	514 (241)
C	Dissolution of η′ and η	661 (388)	686 (413)
D	Secondary phase melting	733 (460)	734 (461)

[1] GP: Guinier–Preston.

It is common knowledge that the concentration of vacancies within a material scales in a positive and proportionate manner with rising temperature. Hence, water quenching from the solutionization temperature thereby locks in an excess concentration of vacancies within the matrix upon cooling to ambient. Ryum and Jiang's models [7–9] highlight the clear importance of these quenched-in vacancies on the precipitation strengthening of 7xxx series alloys. In particular, they highlight the notion that these vacancies will coalesce to create the VRCs required to activate the β precipitation reaction sequence. However, when sizing is applied to the as-quenched product, the associated deformation would annihilate a portion of the quenched-in vacancies by dislocation movement as a result of plastic deformation. This would then lower the volume fraction of VRCs, and in turn, the propensity for GP-zone (II) formation from the β-reaction. This concept was supported by the DSC results, as peak A within the trace acquired from the Sol-Size specimen (Figure 4a) was significantly smaller than that developed from the Size-Sol counterpart (Figure 4b). Furthermore, a suppression of the β-reaction sequence would be expected to increase the magnitude of peak B. In this sense, auxiliary solute atoms would now be available for use within the α precipitation sequence such that higher concentrations of η would now be precipitated directly from the SSSS. This concept was also obvious when comparing the Sol-Size and Size-Sol traces (Figure 4). Similar DSC results have been reported by Ghosh et al. [25] in a study looking at applying high pressure torsion to a 7150 alloy between quench and artificial aging, with a comparable, but much more intense decrease in the peak associated with GP-zone (II) formation along with an increase in intensity in the η′/η peak.

Additional samples were then prepared through the complete processing sequences (Sol-Size-Age and Size-Sol-Age) and run in the DSC (Figure 5). Similar to the data gathered from unaged specimens, the reactions A′–D′ also stem from specific events related to in-situ changes to the underlying precipitates as summarized in Table 4. The first endothermic peak (A′) was associated to the dissolution of GP-zones. It should be noted that this likely involved the dissolution of both GP-zone (I) and GP-zone (II), as these are indistinguishable events. Next, an exothermic doublet peak (B′) was noted. This was attributed to the formation/growth of η′ and formation of η. Similar to the Sol-Size and Size-Sol traces (Figure 4), the endothermic peak (C′) was caused by the dissolution of these precipitates followed by endothermic peak (D′) representing the melting of a secondary phase; again, most likely the S or T phase. When comparing the traces shown in Figure 5, one striking difference was that endothermic peak A′ was substantially smaller in the Sol-Size-Age data. This implied that a lower concentration of GP-zones was present within the starting T6 material, lending further support to the notion that sizing immediately after quench had supressed the formation of a GP-zone (II) through the same mechanism previously discussed. Along with the differences in the A′ peak, a clear doublet is present at peak B′ in the Size-Sol-Age material, where the Sol-Size-Age material showed a slight shoulder in the peak. DeIasi and Adler [28] also saw a similar distinct doublet in AA7075-T651 along with a shoulder in the overaged AA7075-T7351, identifying the first peak as being the formation/growth of η′ as well as η formation and the second peak exclusively a result of η growth. This clear doublet in the Size-Sol-Age material, along with a shoulder in the Sol-Size-Age material, suggests the latter is closer to an overaged condition, with fully developed η present within the microstructure, leading to a reduced likelihood of η growth compared to the Size-Sol-Age material, where fine η formation and growth would take place.

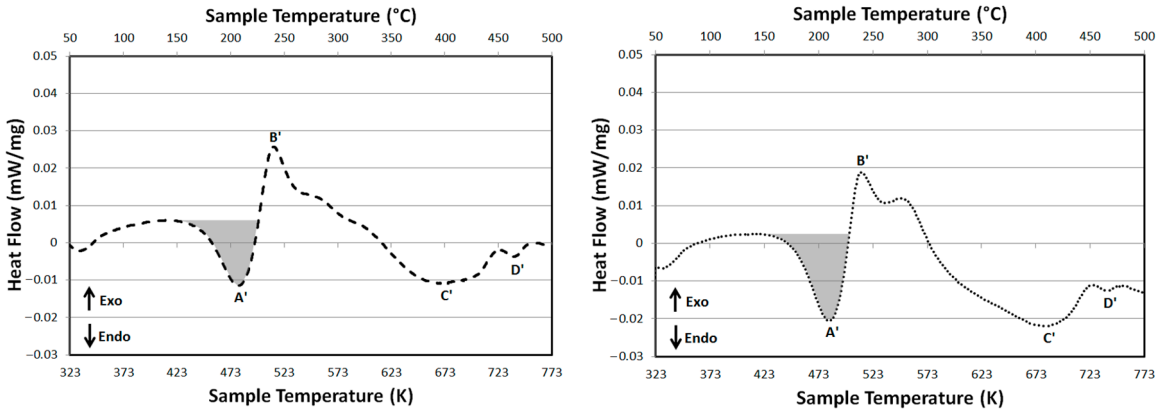

Figure 5. DSC scans recorded from samples of PM7075 after (**a**) Sol-Size-Age and (**b**) Size-Sol-Age processing.

Table 4. Summary of the precipitation events observed in Sol-Size-Age and Size-Sol-Age processed specimens.

Peak	Event Description	Temperature K (°C)	
		Sol-Size-Age	Size-Sol-Age
A′	GP-zone dissolution	480 (207)	483 (210)
B′	η′ and η formation	513 (240)	512 (239)
C′	Dissolution of η′ and η	667 (394)	680 (407)
D′	Secondary phase melting	737 (464)	739 (466)

In an effort to substantiate the DSC findings, more direct evidence on the nature of the precipitates was sought by TEM. Representative BF images of samples processed through Sol-Size-Age and Size-Sol-Age are provided in Figure 6 along with accompanying <112> SADPs in Figure 7. The BF images revealed stark differences between the two samples. The Sol-Size-Age material had precipitates of a high aspect ratio and uniform thickness lying parallel to the {111} planes. These were also quite coarse, with a width in the range of 5–6 nm and length of approximately 11–16 nm. Hence, it was postulated that these represented a plate-like morphology lying on the {111} planes of the aluminum matrix, consistent with the crystallographic orientation of η [7]. In the case of Size-Sol-Age, a much finer, homogenously distributed precipitate structure was observed. Whereas some particles were round (nominal diameter ~2–6 nm), others were thin, rectangular features that lay on {111} planes and had a typical length of 4–6 nm and a uniform thickness (~1 nm). Based on work by Sha and Cerezo [29], η′ will exist as plates on the {111} planes within the α-aluminum matrix. Hence, it was postulated that the rectangular precipitates were in fact plates of η′ viewed edge-on. Overall, the general appearance of the precipitates within the Size-Sol-Age material was in strong agreement with that found for wrought AA7075-T6 by Guo et al. [30].

Beyond the BF images themselves, the corresponding electron diffraction patterns aligned close to the <112> axis for each sample also showed clear evidence that a secondary phase was present (Figure 7). In the case of the Sol-Size-Age material (Figure 7a), this came in the form of distinct secondary diffraction points that were thereby attributed to the presence of semi-coherent/incoherent precipitates. The secondary diffraction points lay in rows parallel to the <111> directions (indicated by arrow in Figure 7a), such that the resultant pattern was in strong agreement with SADPs devised by Hansen et al. for an Al–Zn–Mg alloy containing η′ and η phases [10]. In the SADP recorded from the Size-Sol-Age product (Figure 7b), discrete secondary diffraction spots were less obvious, and relatively intense streaking within the pattern was present (location and direction shown in Figure 7b by arrow), indicating that the diffracting phase now maintained an increased level of coherency with the

α-aluminum matrix. This implied that fully coherent GP-zones and/or the semi-coherent precipitate η′ now dominated the structure.

Based on the combination of TEM and DSC findings, the Size-Sol-Age material appeared to have a microstructure largely comprised of an α-aluminum matrix along with a combination of GP-zone and η′ precipitates. This differed from the Sol-Size-Age material, as it was effectively in an overaged state given the increased size of the precipitates and a more acute presence of the fully incoherent η phase within the microstructure. These microstructural differences were in direct agreement with the hardness results (Figure 3), as the Sol-Size-Age material was measurably softer.

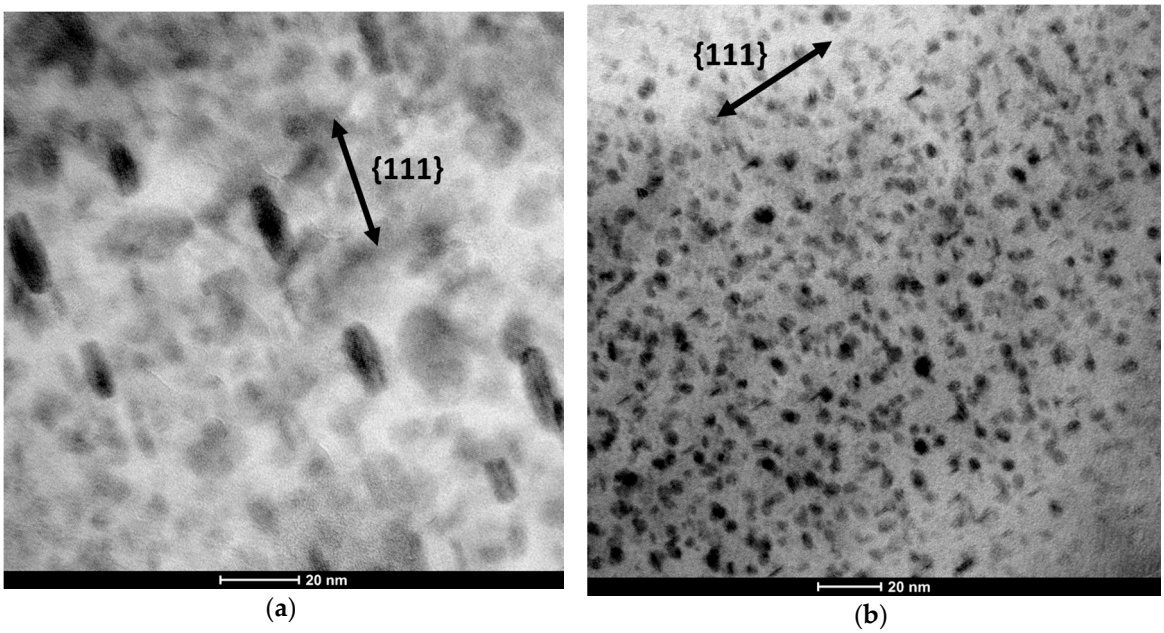

Figure 6. Bright field (BF) TEM images of (**a**) Sol-Size-Age and (**b**) Size-Sol-Age processed samples with the beam closely aligned to the <112> zone axis.

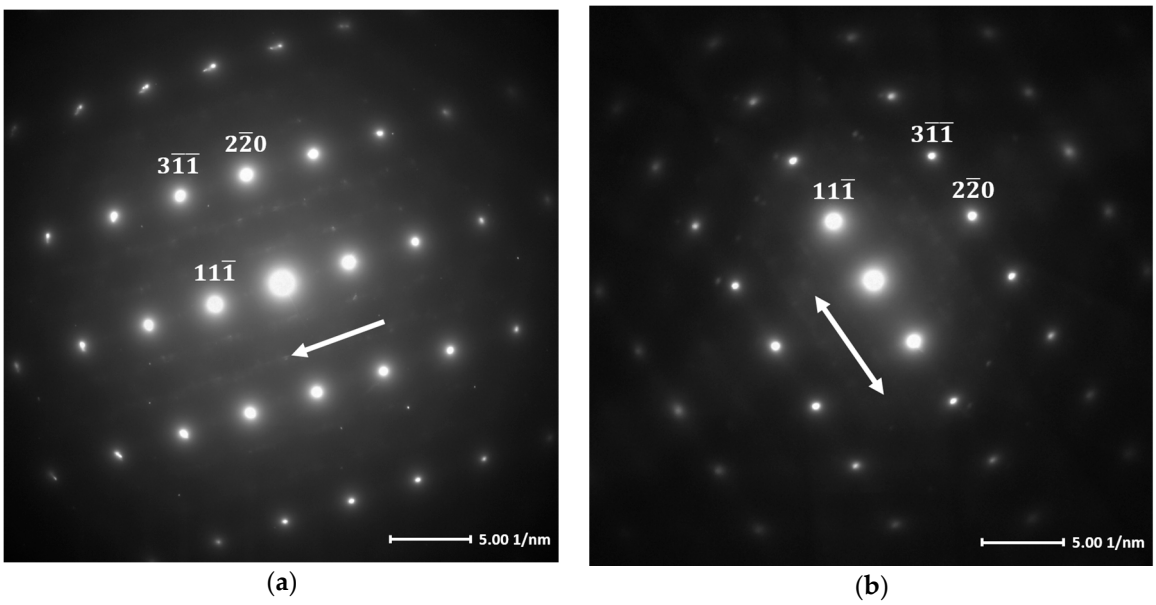

Figure 7. Selected area diffraction patterns (SADPs) recorded from (**a**) Sol-Size-Age and (**b**) Size-Sol-Age processed samples with the beam closely aligned to the <112> zone axis.

3.2.2. Fatigue Testing

In the next phase of testing, the fatigue performance of PM7075 was evaluated under the different processing streams of interest. A summary of the staircase results is presented in Table 5. The highest fatigue durability was noted when sizing was applied before the full heat-treatment cycle. Here, sizing was found to invoke a minor gain in fatigue strength (~5%) relative to the specimens processed without any sizing at all (Sol-Age). Prior data indicated that these two materials were comparable in terms of bulk density and hardness (Figure 3), presumably eliminating these attributes as influential factors. The one tangible difference was in that of surface roughness (Figure 2), whereby an improved value was noted for the Size-Sol-Age products compared to those of Sol-Age. This equated to a smoother exterior surface that would have contained a reduced presence of crack-inducing surface asperities and benefitted fatigue durability. It was also possible that sizing had closed a portion of the near-surface porosity, which has been shown to act as fatigue crack initiation sites within other aluminum PM materials [31]. Overall, it was concluded that the surface condition differential was a key factor of influence.

Table 5. Fatigue strength of PM7075 after the application of Sol-Age, Sol-Size-Age, and Size-Sol-Age processing.

Process	σ_a (50%) [1] (MPa)	n [2]	SD [3] (MPa)	vs. Sol-Age
Sol-Age	218	14	5	-
Size-Sol-Age	228	10	4	+5%
Sol-Size-Age	168	10	4	−23%

[1] Fatigue strength (σ_a): 50% passing as determined through MPIF Standard 56; [2] Number of samples tested (n); [3] Standard deviation (SD) calculated in accordance with MPIF Standard 56.

Interestingly, a large decrease in fatigue behaviour ensued when sizing was implemented as an intermediate step between solutionization/quench and aging. When comparing the metallurgical attributes of the Sol-Size-Age and Size-Sol-Age specimens assessed to this point, the principal difference was a reduced hardness (Figure 3) as driven by changes in the strengthening precipitates present (Figure 6). As such, a drop in fatigue performance seemed logical. However, given the magnitude of the fatigue decline, it was prudent to complete additional characterization work to determine if auxiliary factors were at play. In particular, it was prudent to determine if sizing-derived microcracks and/or different states of residual stress existed within the materials. Regarding the former, the manner of sizing applied clearly resulted in plastic deformation. Furthermore, it was conceivable that this would be more acute at the surfaces of the bar, as lateral flow would be less constrained here than at regions within the bulk interior. This scenario could thereby facilitate microcracking and a concomitant decline in fatigue performance. To assess this possibility, specimens produced by Sol-Size-Age and Size-Sol-Age were mounted, polished, and examined extensively at high magnifications by SEM. No evidence of microcracking was discovered in any of these specimens, thereby confirming that this was not a contributing factor.

In standard T6 (i.e., Sol-Age) processing, it is well documented that 7xxx series aluminum alloys will have compressive residual stress within the surface of the part instilled by quenching after solution heat-treatment [32,33]. Such stresses are beneficial to fatigue behaviour, as they act to resist in-service tensile loads. During solution heat-treatment, the large thermal gradients created from water quenching from the solutionization temperature result in the surface of the sample cooling quicker than that of the interior. Once the interior begins to cool, the surface material will resist thermal contraction of the inner material, so that the surface is ultimately in a state of compression while the interior is in tension. The measured surface in-plane residual stresses within the samples processed by Sol-Size-Age and Size-Sol-Age are shown in Figure 8. It can be seen that Sol-Size-Age yielded a product with a lower level of compressive surface residual stress. This drop upon sizing after quench was believed to be caused by the plastic deformation acting similar to a stress-relieving process (such as stretching). With regard to Size-Sol-Age processing with the sizing operation performed prior to the

heat-treatment, the developed residual stresses within the compact are solely a result of the thermal gradients developed during quenching, and should therefore be similar to the case of a standard T6 treatment.

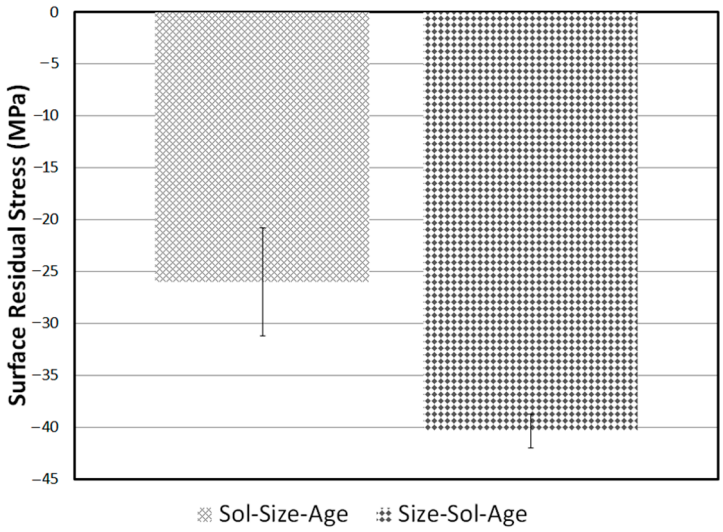

Figure 8. Surface residual stress measured in PM7075 as a result of Sol-Size-Age and Size-Sol-Age processing.

In the case of Sol-Size-Age processing, it was plausible that the reduction in this advantageous attribute had contributed to the noted decline in fatigue strength in the samples, along with the previously discussed effects of precipitation hardening differences within the system.

To determine if the fatigue differences were unique to PM7075, equivalent processing/testing was completed on the wrought counterpart AA7075. Here, test bars of the material were processed through Sol-Age and Sol-Size-Age sequences, utilizing the same sizing pressure applied during PM7075 Sol-Size-Age processing (400 MPa). The resultant data on fatigue performance are given in Table 6. Akin to PM7075, Sol-Size-Age processing again resulted in lower fatigue strength. However, the drop was much less pronounced, which implied that the underlying mechanism was exacerbated in the PM system and/or that additional factors were contributing. As would be expected, the wrought alloy exhibited considerably higher fatigue strengths relative to the data previously acquired for the PM products studied (Table 5).

Table 6. Fatigue strength of wrought AA7075 processed to Sol-Age and Sol-Size-Age conditions.

Process	σ_a (50%) [1] (MPa)	n [2]	SD [3] (MPa)	vs. Sol-Age
Sol-Age	366	12	9	-
Sol-Size-Age	344	10	5	−6%

[1] Fatigue strength: 50% passing as determined through MPIF Standard 56; [2] Number of samples tested; [3] Standard deviation calculated in accordance with MPIF Standard 56.

It was postulated that these transitions in fatigue behaviour were underpinned by fundamental differences in microstructure. In this sense, aluminum PM and wrought materials differ in that the former contain higher concentrations of porosity as well as a network of oxides that stems from the starting raw powders. As both attributes are known to serve as preferential sites for crack initiation and thereby lower fatigue resistance, the general inferiority of PM7075 was as expected. However, these same features would also serve as stress concentrators during deformation (i.e., sizing). This would thereby prompt localized increases in the extent of plastic deformation, and concomitantly abnormally high levels of vacancy annihilation within their vicinity. The capacity to form vacancy rich clusters (VRC) would then be heterogeneously reduced, and in turn, so too would the net concentration of the most influential strengthening precipitate, GP-zone (II), as formed through the β-reaction sequence.

This scenario would preferentially weaken the alloy near pores and oxides so as to further exacerbate the ease at which fatigue cracks would nucleate and grow. Given that wrought AA7075 is largely devoid of porosity and oxide networks, Sol-Size-Age processing thereby imparted a more prolific fatigue decline in the PM material.

3.3. Effects of Shot Peening

Beyond sizing and heat-treatment, shot peening is also considered as a secondary operation widely utilized and accepted in industry to combat fatigue-based failure within materials. Given the aforementioned trends in fatigue behaviour, emphasis was restricted to the most advantageous means of processing PM7075: Size-Sol-Age. With shot peening applied to the specimens, an increase in fatigue strength of 29% compared to the unpeened counterpart was found (Table 7). These gains in fatigue strength can be attributed to the induced compressive residual stresses caused by inner material resisting the plastic deformation as a result of shot impacting the surface of the sample. The surface in-plane residual stress was measured by XRD (as described in Section 2) to be −297 MPa (standard deviation 8 MPa), which has been shown to persist to a depth of approximately 80 µm in samples processed and peened in a similar manner [34]. This ≈30% increase in fatigue strength from shot peening was also in line with similar studies completed through rotating–bending fatigue [21] as well as published results for wrought 7075 [16,18,35] (showing 20–50% gains).

Table 7. Effect of shot peening on the fatigue strength of Size-Sol-Age processed specimens of PM7075.

Process	σ_a (50%) [1] (MPa)	n [2]	SD [3] (MPa)	vs. Size-Sol-Age
Size-Sol-Age-Peen	294	10	4	+29%

[1] Fatigue strength: 50% passing as determined through MPIF Standard 56; [2] Number of samples tested; [3] Standard deviation calculated in accordance with MPIF Standard 56.

3.4. Effects of Thermal Exposure

It is well-understood that thermal exposure is a problematic operating condition for 7xxx aluminum alloys. For instance, when temperatures approach or exceed that utilized for aging (398 K, 125 °C), precipitation and coarsening of the η phase is exacerbated, leading to in-situ over-aging and a concomitant decline in mechanical properties. Likewise, if the alloy is shot peened, the associated fatigue gains can deteriorate during thermal exposure via a relaxation of the underpinning compressive residual stress. It is for this reason that a maximum operating temperature of 366 K (93 °C) is recommended for shot-peened aluminum alloys [36]. Hence, the effects of thermal exposure at temperatures below (353 K, 80 °C) and above (433 K, 160 °C) these important thresholds were assessed.

Commencing with tensile testing, samples were processed into the Sol-Age condition and exposed. Sizing was not considered in these particular tests, as the machining needed to convert the sized rectangular blank into a round bar would completely remove the sized surface, thereby omitting the development of an accurate correlation to the effects of this process variable. The resultant tensile data are shown in Table 8. Exposure at 353 K (80 °C) for 1000 h imparted minimal changes. A higher thermal exposure of 433 K (160 °C) showed a drastic decrease in both yield and ultimate tensile strength coupled with a significant increase in elongation to fracture. Such differences were expected, since the higher temperature should have facilitated excessive over-aging. This was substantiated through XRD analyses (Figure 9), as the 353 K (80 °C) sample only exhibited diffraction peaks that matched the α-aluminum matrix phase. No evidence of the incoherent η phase was detected within the system, indicating that the material remained in a peak hardened state. This was as expected given that the exposure temperature was well below the aging temperature applied during Sol-Age processing (398 K, 125 °C). Conversely, the 433 K (160 °C) exposure samples showed distinct diffraction peaks that corresponded to η ($MgZn_2$). As such, the material had most certainly over-aged under these conditions synonymous with the steep decline in tensile properties (Table 8).

Table 8. Effects of thermal exposure (1000 h at indicated temperature) on the tensile properties of PM7075 initially processed into the Sol-Age condition.

Process	σ_{yield} [1] (MPa)	σ_{UTS} [2] (MPa)	E [3] (GPa)	Elongation [4] (%)
Sol-Age	466 ± 7	496 ± 9	64.7 ± 2.4	1.5 ± 0.2
Sol-Age + 353 K (80 °C)	474 ± 14	480 ± 20	65.1 ± 1.5	1.1 ± 0.5
Sol-Age + 433 K (160 °C)	237 ± 4	323 ± 8	64.5 ± 2.5	4.3 ± 0.6

[1] Yield stress at 0.2% strain offset; [2] Ultimate tensile strength; [3] Young's modulus of elasticity; [4] Total engineering strain to fracture.

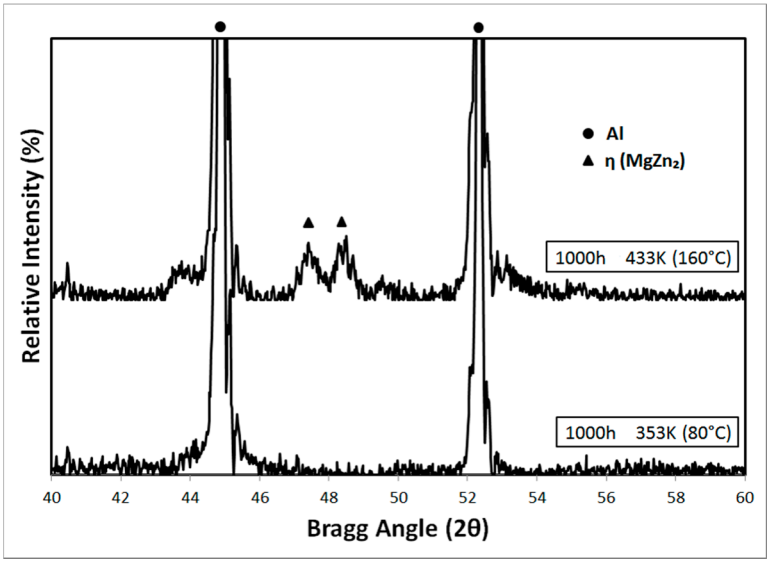

Figure 9. XRD (X-ray diffraction) traces acquired from Sol-Age samples exposed to 353K (80 °C) and 433K (160 °C) for 1000 h.

Data illustrating the effects of thermal exposure on the fatigue of samples originally processed into the Size-Sol-Age state are shown in Table 9. Those exposed to 353 K (80 °C) showed no apparent loss in fatigue performance consistent with the trends in tensile data (Table 8). Interestingly, this same exposure temperature actually invoked a measurable decrease in fatigue performance for the Size-Sol-Age-Peen specimens, declining from 294 MPa (Table 7) to 260 MPa (representing a loss of ≈12% fatigue strength). As exposure at 353 K (80 °C) progressed, it was determined that a gradual reduction in residual stress also occurred (Figure 10). This culminated in a final level of −200 MPa, which represented a loss of ≈30%. Hence, it was presumed that this was the principal factor responsible given that no changes to the underlying precipitate structure were anticipated under these conditions per the data in Table 8 and Figure 9.

Upon exposure to 433 K (160 °C), a significant reduction in fatigue strength was seen in the Size-Sol-Age-Peen material, dropping to 173 MPa from 294 MPa (Table 7), representing a loss of approximately 41% due to the elevated temperature exposure. This significant drop in fatigue strength is due to a combination of over-aging of the material (supported by tensile and XRD analysis, Table 8 and Figure 9) along with an essentially full relaxation of the compressive residual stresses imparted by shot peening. As shown in Figure 10, we can see that the Size-Sol-Age-Peen material dropped from a starting compressive residual stress value of ≈310 MPa to ≈40 MPa after 1000 h at 433 K (160 °C) with all the peening-induced residual stress wiped out, resulting in a level approximately equal to the residual stress resulting solely from the heat-treatment process (Figure 8).

Table 9. Fatigue strength of thermally exposed PM7075 Size-Sol-Age and Size-Sol-Age-Peen.

Process	σ_a (50%) [1] (MPa)	n [2]	SD [3] (MPa)	vs. Size-Sol-Age
Size-Sol-Age 353 K (80 °C)	225	10	4	−1%
Size-Sol-Age-Peen 353 K (80 °C)	260	10	4	+14%
Size-Sol-Age-Peen 433 K (160 °C)	173	10	4	−24%

[1] Fatigue strength: 50% passing as determined through MPIF Standard 56; [2] Number of samples tested; [3] Standard deviation calculated in accordance with MPIF Standard 56.

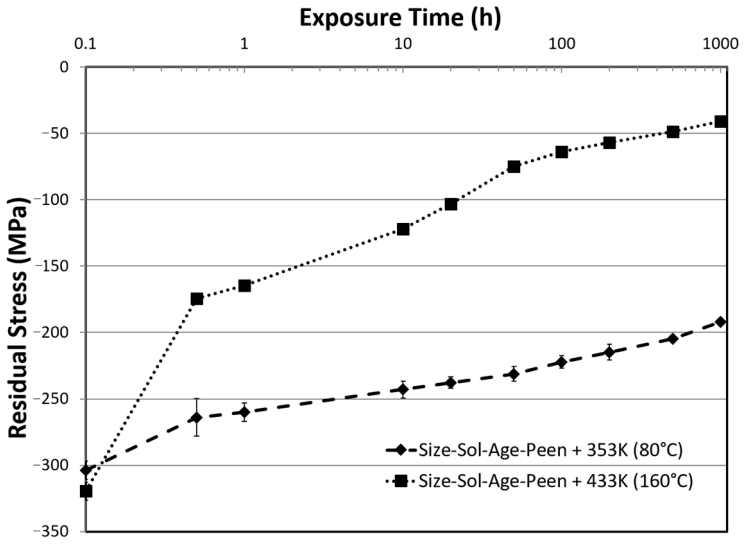

Figure 10. Residual stress as a function of elevated temperature exposure for Size-Sol-Age-Peen samples.

4. Conclusions

The application of post-sinter sizing, heat-treatment, and shot peening operations to PM7075 was studied in this work. Each process influenced the finished product such that the following conclusions could be drawn:

1. Sizing reduced the surface roughness (*S*q) in all scenarios considered from ≈50 μm to ≈15 μm, but did not impart a measurable change in the density of the finished products.
2. When test bars were sized in the T1 state and then heat-treated to the T6 condition, the product exhibited a slight gain in fatigue strength (~5%) relative to the standard unsized counterpart. This small gain was principally attributed to the improved surface roughness instilled through sizing.
3. If sizing was applied directly after quenching, the product exhibited declines in apparent hardness (~7 HRB) and fatigue strength (−23%) relative to the unsized counterpart. It was determined that sizing in this manner had catalyzed precipitate growth, leading to larger precipitates and an increased concentration of incoherent η in the product. This processing sequence was also found to have reduced the compressive residual stress from −40 MPa to −25 MPa.
4. Shot peening successfully instilled a relatively large compressive residual stress at the surface of PM7075 (−293 MPa) that improved 3-point bending fatigue by 29%. However, these gains were weakened by thermal exposure at 358 K (80 °C), and completely eliminated when the temperature was raised to 433 K (160 °C).

Acknowledgments: The authors would like to acknowledge the Auto21 Networks of Centres of Excellence and the Natural Sciences and Engineering Research Council of Canada (NSERC), for financial support via grant C502-CPM and the doctoral post-graduate scholarship program. Bernd Mais (Ecka Granules) is acknowledged for the provision of the Alumix 431D powder employed, along with William Caley, Arjun Kaushal, and Abdul Kahn of the Manitoba Institute for Materials (University of Manitoba, Winnipeg, MB, Canada) for help with the TEM work.

Author Contributions: Matthew David Harding and Donald Paul Bishop conceived and designed the experiments with industrial input from Ian William Donaldson and Rich Lester Hexemer Junior All experimental work was completed by Matthew David Harding apart from the industrial sintering completed by Ian William Donaldson and Rich Lester Hexemer Junior. Matthew David Harding and Donald Paul Bishop analyzed the data and wrote the paper, with Ian William Donaldson and Rich Lester Hexemer Junior providing input upon editing the initial draft.

Conflicts of Interest: The authors declare no conflict of interest.

References

1. Boland, C.D.; Hexemer, R.L.; Donaldson, I.W.; Bishop, D.P. Development of an aluminum PM alloy for 'press-sinter-size' technology. *Int. J. Powder Metall.* **2011**, *47*, 39–48.
2. Cooke, R.W.; Hexemer, R.L.; Donaldson, I.W.; Bishop, D.P. Press-and-sinter processing of a PM counterpart to wrought aluminum 2618. *J. Mater. Process. Technol.* **2016**, *230*, 72–79. [CrossRef]
3. Heard, D.W.; Donaldson, I.W.; Bishop, D.P. Metallurgical assessment of a hypereutectic aluminum-silicon P/M alloy. *J. Mater. Process. Technol.* **2009**, *209*, 5902–5911. [CrossRef]
4. LaDelpha, A.D.P.; Neubing, H.; Bishop, D.P. Metallurgical assessment of an emerging Al-Zn-Mg-Cu P/M alloy. *Mater. Sci. Eng. A* **2009**, *520*, 105–113. [CrossRef]
5. Schaffer, G.B.; Huo, S.H. On development of sintered 7xxx series aluminum alloys. *Powder Metall.* **1999**, *42*, 219–226. [CrossRef]
6. Mondolfo, L.F.; Gjostein, N.A.; Levinson, D.W. Structural Changes during the Aging in an Al-Mg-Zn Alloy. *JOM* **1956**, *8*, 1378–1385. [CrossRef]
7. Ryum, N. Precipitation Kinetics in an Al-Zn-Mg-Alloy. *Z. Met.* **1975**, *66*, 338–343.
8. Ryum, N. Further Investigation on the Precipitation Kinetics in an Al-Zn-Mg-Alloy. *Z. Met.* **1975**, *66*, 344–346.
9. Jiang, X.J.; Noble, B.; Holme, B.; Waterloo, G.; Tafto, J. Differential Scanning Calorimetry and Electron Diffraction Investigation on Low-Temperature Aging in Al-Zn-Mg Alloys. *Metall. Mater. Trans. A* **2000**, *31*, 339–348. [CrossRef]
10. Hansen, V.; Stiller, K.; Waterloo, G.; Gjonnes, J.; Li, X.Z. Structure and Transformations during Artificial Aging of an Industrial 7xxx-Series Al-Zn-Mg-Zr Alloy. *Mater. Sci. Forum* **2002**, *396–402*, 815–820. [CrossRef]
11. Liu, J.; German, R.M. Densification and Shape Distortion in Liquid-Phase Sintering. *Metall. Mater. Trans. A* **1999**, *30*, 3211–3217. [CrossRef]
12. Yuan, X.N.; Huo, S.H.; Schaffer, G.B.; Qian, M. Distortion in a 7xxx Aluminum Alloy during Liquid Phase Sintering. *Metall. Mater. Trans. A* **2014**, *45*, 1010–1018. [CrossRef]
13. Cooke, R.W.; Bishop, D.P.; Hexemer, R.L.; Donaldson, I.W. Effects of Zirconium Additions on the Sintering Response of an Aluminum–Copper–Magnesium Alloy. *Int. J. Powder Metall.* **2013**, *49*, 37–46.
14. Papazian, J.M. A Calorimetric study of precipitation in aluminum alloy 2219. *Metall. Trans. A* **1981**, *12*, 269–280. [CrossRef]
15. Deschamps, A.; Livet, F.; Bréchet, Y. Influence of Predeformation on Ageing in an Al-Zn-Mg alloy—I. Microstructure Evolution and Mechanical Properties. *Acta Mater.* **1999**, *47*, 281–292. [CrossRef]
16. Was, G.S.; Pelloux, R.M. The Effect of Shot Peening on the Fatigue Behavior of Alloy 7075-T6. *Metall. Trans. A* **1979**, *10*, 656–658. [CrossRef]
17. Was, G.S.; Pelloux, R.M.; Frabolot, M.C. Effect of Shot Peening Methods on the Fatigue of Alloy 7075-T6. In Proceedings of the 1st International Conference on Shot Peening, Paris, France, 14–17 September 1981; pp. 445–451.
18. Benedetti, M.; Fontanari, V.; Scardi, P.; Ricardo, C.L.A.; Bandini, M. Reverse bending fatigue of shot peened 7075-T651 aluminium alloy: The role of residual stress relaxation. *Int. J. Fatigue* **2009**, *31*, 1225–1236. [CrossRef]
19. Wagner, L.; Mhaede, M.; Wollmann, M.; Altenberger, I.; Sano, Y. Surface layer properties and fatigue behavior in Al 7075-T73 and Ti-6Al-4V Comparing results after laser peening, Shot peening and ball-burnishing. *Int. J. Struct. Integr.* **2011**, *2*, 185–199. [CrossRef]
20. Honda, T.; Ramulu, M.; Kobayshi, A.S. Shot Peening and Fatigue Crack Growth in 7075-T7351 Aluminum. *Key Eng. Mater.* **2005**, *297–300*, 72–77. [CrossRef]

21. Harding, M.D.; Bishop, D.P.; Donaldson, I.W. Effects of Shot Peening on Aluminum Powder Metallurgy Alloys. In *Advances in Powder Metallurgy and Particulate Materials, Proceedings of the 2010 International Conference on Powder Metallurgy and Particulate Materials, Ft. Lauderdale, FL, USA, 27–30 June 2010*; Metal Powder Industries Federation: Princeton, NJ, USA, 2010; pp. 629–640.
22. Metal Powder Industries Federation. *Determination of Density of Compacted or Sintered Powder Metallurgy (PM) Products*; MPIF Standard 42; MPIF: Princeton, NJ, USA, 2008.
23. Metal Powder Industries Federation. *Determination of Rotating Beam Fatigue Endurance Limit of Powder Metallurgy (PM) Materials*; MPIF Standard 56; MPIF: Princeton, NJ, USA, 2011.
24. ASTM International. *Standard Test Method for Tension Testing of Metallic Materials*; ASTM E8M-07; ASTM International: West Conshohocken, PA, USA, 2007.
25. Gosh, K.S.; Gao, N.; Starink, M.J. Characterization of high pressure torsion processed 7150 Al-Zn-Mg-Cu alloy. *Mater. Sci. Eng. A* **2012**, *552*, 164–171. [CrossRef]
26. Berg, L.K.; Gjønnes, J.; Hansen, V.; Li, X.Z.; Knutson-Wedel, M.; Waterloo, G.; Schryvers, D.; Wallenberg, L.R. GP-zones in Al-Zn-Mg alloys and their role in artificial aging. *Acta Mater.* **2001**, *49*, 3443–3451. [CrossRef]
27. Wang, D.; Ni, D.R.; Ma, Z.Y. Effect of pre-strain and two-step aging on microstructure and stress corrosion cracking of 7050 alloy. *Mater. Sci. Eng. A* **2008**, *494*, 360–366. [CrossRef]
28. Delasi, R.; Adler, P. Calorimetric Studies of 7000 Aluminum Alloys: I. Matrix Precipitate Characterization of 7075. *Metall. Trans. A* **1977**, *8*, 1177–1183.
29. Sha, G.; Cerezo, A. Early-stage precipitation in Al-Zn-Mg-Cu alloy (7050). *Acta Mater.* **2004**, *52*, 4503–4516. [CrossRef]
30. Guo, W.; Guo, J.; Wang, J.; Yang, M.; Li, H.; Wen, X.; Zhang, J. Evolution of precipitate microstructure during stress aging of an Al-Zn-Mg-Cu alloy. *Mater. Sci. Eng. A* **2015**, *634*, 167–175. [CrossRef]
31. Grayson, G.N.; Schaffer, G.B.; Griffiths, J.R. Fatigue crack propagation in a sintered 2xxx series aluminium alloy. *Mater. Sci. Eng. A* **2006**, *434*, 1–6. [CrossRef]
32. Robinson, J.S.; Tanner, D.A.; van Petegem, S.; Evans, A. Influence of quenching and aging on residual stress in Al-Zn-Mg-Cu alloy 7449. *Mater. Sci. Technol.* **2012**, *28*, 420–430. [CrossRef]
33. Robinson, J.S.; Tanner, D.A.; Truman, C.E.; Paradowska, A.M.; Wimpory, R.C. The influence of quench sensitivity on residual stresses in the aluminium alloys 7010 and 7075. *Mater. Charact.* **2012**, *65*, 73–85. [CrossRef]
34. Harding, M.D.; Donaldson, I.W.; Hexemer, R.L.; Gharghouri, M.A.; Bishop, D.P. Characterization of the microstructure, mechanical properties, and shot peening response of an industrially processed Al-Zn-Mg-Cu PM alloy. *J. Mater. Process. Technol.* **2015**, *221*, 31–39. [CrossRef]
35. ASM International. *ASM Handbook Volume 5: Surface Engineering*; ASM International: Materials Park, OH, USA, 1994; pp. 278–302.
36. Society of Automotive Engineers, Inc. *SAE Manual on Shot Peening HS-84*; Society of Automotive Engineers, Inc.: Warrendale, PA, USA, 2001.